# Seeding Supermassive Black Holes with Self-interacting Dark Matter: A Unified Scenario with Baryons

Wei-Xiang Feng[1] , Hai-Bo Yu[1] , and Yi-Ming Zhong[2] 
[1] Department of Physics and Astronomy, University of California, Riverside, CA 92521, USA; wfeng016@ucr.edu, haiboyu@ucr.edu
[2] Kavli Institute for Cosmological Physics, University of Chicago, Chicago, IL 60637, USA; ymzhong@kicp.uchicago.edu

## Abstract

Observations show that supermassive black holes (SMBHs) with a mass of $\sim 10^9 \, M_\odot$ exist when the universe is just 6% of its current age. We propose a scenario where a self-interacting dark matter halo experiences gravothermal instability and its central region collapses into a seed black hole. The presence of baryons in protogalaxies could significantly accelerate the gravothermal evolution of the halo and shorten collapse timescales. The central halo could dissipate its angular momentum remnant via viscosity induced by the self-interactions. The host halo must be on high tails of density fluctuations, implying that high-$z$ SMBHs are expected to be rare in this scenario. We further derive conditions for triggering general relativistic instability of the collapsed region. Our results indicate that self-interacting dark matter can provide a unified explanation for diverse dark matter distributions in galaxies today and the origin of SMBHs at redshifts $z \sim 6$–7.

*Unified Astronomy Thesaurus concepts:* Supermassive black holes (1663); Dark matter (353)

## 1. Introduction

Astrophysical observations of high-redshift quasars indicate that $\sim 10^9 \, M_\odot$ black holes exist when the universe is just 800 Myr old after the Big Bang ($z \sim 7$); see Inayoshi et al. (2020) for a review. The origin of these supermassive black holes (SMBHs) is still a mystery. In particular, it is extremely puzzling how they could become so massive in such a short time. A popular idea is that there exist heavy seed black holes in the early universe and they grow massive by accreting baryons (Volonteri 2010; Natarajan 2011). Assuming Eddington accretion, we can relate the black hole mass ($M_{\rm BH}$) and its seed mass ($M_{\rm seed}$) as (Salpeter 1964)

$$M_{\rm BH} = M_{\rm seed} \exp(\Delta t / \tau), \tag{1}$$

where $\Delta t$ is the elapse time and $\tau = (450/f_{\rm Edd})[\epsilon_M/(1 - \epsilon_M)]$Myr is the e-folding time. $\epsilon_M$ is the radiative efficiency and commonly assumed to be 0.1 (Shakura & Sunyaev 1976), and $f_{\rm Edd}$ is the Eddington ratio following $f_{\rm Edd} = L_{\rm bol}/L_{\rm Edd}$, where $L_{\rm bol}$ is the observed bolometric luminosity and $L_{\rm Edd} = 1.3 \times 10^{38}(M_{\rm BH}/M_\odot)$erg s$^{-1}$ is the Eddington luminosity. $\epsilon_M$ measures the efficiency of conversion of mass energy to luminous energy by accretion, while $f_{\rm Edd}$ characterizes the efficiency of accretion luminosity.

Consider J1007+2115, the most massive known quasar with $M_{\rm BH} \approx 1.5 \times 10^9 \, M_\odot$ at $z > 7.5$ (Yang et al. 2020b). Taking $f_{\rm Edd} \simeq 1$, we estimate $M_{\rm seed} \sim 10^4 \, M_\odot$ if it forms at $z \sim 30$, i.e., $\Delta t = 597$ Myr to its observed $z = 7.51$. Such a seed is too massive to be produced from collapsed Population III stars (Inayoshi et al. 2020), but it could form through the direct collapse of pristine baryonic gas (Bromm & Loeb 2003; Begelman et al. 2006); see also Freese et al. (2010). The latter scenario predicts $M_{\rm seed} \sim 10^5$–$10^6 \, M_\odot$. However, observations show there are high-$z$ SMBHs with $f_{\rm Edd}$ much less than 1 (Matsuoka et al. 2019; Onoue et al. 2019). For example, J1205−0000 is observed at $z = 6.7$ with $M_{\rm BH} = 2.2 \times 10^9 \, M_\odot$ and $f_{\rm Edd} = 0.16$ (Onoue et al. 2019). The Eddington accretion then implies it grows from a seed with a mass

of $2 \times 10^8 \, M_\odot$ at $z \sim 30$, too heavy to be produced via the direct collapse of gas.

There could be complications in those estimates. For example, the accretion luminosity may not be a constant over time, and SMBHs could experience a rapid accretion phase beyond the Eddington limit (Begelman 1979; Volonteri & Rees 2005; Alexander & Natarajan 2014). In addition, the radiative efficiency depends on black hole spin. For standard thin disks, which drive the hole to maximal spin, $\epsilon_M \sim 0.42$, while for magnetohydrodynamic disks $\epsilon_M \sim 0.2$ (Shapiro 2005) or even lower $\epsilon_M \sim 0.01$ associated with super-Eddington accretion (McKinney et al. 2014; Sadowski et al. 2015). Furthermore, mergers could amplify the black hole mass. It's possible that the existence of SMBHs can be explained after taking into account these effects, but more work is needed to understand how they affect individual ones; see Inayoshi et al. (2020) for further discussion.

In this Letter, we study the scenario of gravothermal collapse of self-interacting dark matter (SIDM; Spergel & Steinhardt 2000; Kaplinghat et al. 2016; Tulin & Yu 2018) in explaining the origin of high-$z$ SMBHs. Dark matter self-interactions can transport heat in the halo over cosmological timescales (Dave et al. 2001; Ahn & Shapiro 2005; Vogelsberger et al. 2012; Rocha et al. 2013). As a gravothermal system, the SIDM halo has negative heat capacity (Lynden-Bell & Wood 1968). The central region could become hot and collapse to a singular state with a finite mass at late stages of the evolution (Balberg & Shapiro 2002; Balberg et al. 2002). Thus SIDM has a natural mechanism in triggering dynamical instability, a necessary condition to form a black hole. Recent studies also show that SIDM is favored for explaining diverse dark matter distributions over a wide range of galactic systems; see Tulin & Yu (2018) for a review. It is intriguing to explore an SIDM scenario that may explain the origin of the high-$z$ SMBHs and observations of galaxies at $z \sim 0$.

We adopt a typical baryon mass profile for high-$z$ protogalaxies, and show the collapse time can be shortened by a factor of 100, compared to the SIDM-only case. Even for the self-scattering cross section per unit mass $\sigma/m \sim 1$ cm$^2$ g$^{-1}$, broadly consistent with the value used to explain galactic

observations (Tulin & Yu 2018), the central halo could collapse sufficiently fast to form a seed for $z \gtrsim 7$. Depending on the halo mass, this scenario could explain the origin of high-$z$ SMBHs with $f_{Edd} \sim 1$ and 0.1. It also has a built-in mechanism to dissipate angular momentum remanent of the central halo, i.e., viscosity induced by the self-interactions. We will further show when the 3D velocity dispersion of SIDM particles in the collapsed central region reaches $0.57c$, the general relativistic (GR) instability can be triggered. We demonstrate a unified SIDM scenario that could explain observations of galaxies today and high-$z$ SMBHs. In the appendices, we provide additional information.

## 2. Gravothermal Evolution

We use a conducting fluid model (Balberg et al. 2002; Koda & Shapiro 2011) to study the gravothermal evolution of an SIDM halo, as it yields high resolution for us to closely trace the collapse process. To capture the influence of baryons, we extend the original model with a baryonic component. The evolution of the halo can be described by the following equations:

$$\frac{\partial M_\chi}{\partial r} = 4\pi r^2 \rho_\chi, \quad \frac{\partial(\rho_\chi \nu_\chi^2)}{\partial r} = -\frac{G(M_\chi + M_b)\rho_\chi}{r^2},$$

$$\frac{\partial L_\chi}{\partial r} = -4\pi\rho_\chi r^2 \nu_\chi^2 D_t \ln\frac{\nu_\chi^3}{\rho_\chi}, \quad \frac{L_\chi}{4\pi r^2} = -\kappa\frac{\partial(m\nu_\chi^2)}{k_B \partial r}, \quad (2)$$

where $M_\chi$, $\rho_\chi$, $\nu_\chi$, and $L_\chi$ are dark matter mass, density, 1D velocity dispersion, and luminosity profiles, respectively, and they are dynamical variables and evolve with time; $M_b$ is the baryon mass profile in the host galaxy; $k_B$ is the Boltzmann constant; $G$ is the Newton constant; and $D_t$ denotes the Lagrangian time derivative. Heat conductivity of the dark matter fluid $\kappa$ can be expressed as $\kappa = (\kappa_{lmfp}^{-1} + \kappa_{smfp}^{-1})^{-1}$, where $\kappa_{lmfp} \approx 0.27C\rho_\chi \nu_\chi^3 \sigma k/(Gm^2)$ and $\kappa_{smfp} \approx 2.1\nu_\chi k/\sigma$ denote conductivity in the long- and short-mean-free-path regimes, respectively, and we set $C \simeq 0.75$ based on calibrations with $N$-body simulations (Pollack et al. 2015; Essig et al. 2019). In the short-mean-free-path regime, heat conduction can be characterized by the self-interaction mean free path $\lambda = m/\rho_\chi \sigma$ and $Kn = \lambda/H < 1$, where $H = (\nu_\chi^2/4\pi G\rho_\chi)^{1/2}$ is the scale height. In the long-mean-free-path regime, it is characterized by $H$ and $Kn > 1$.

We assume the *initial* halo follows a Navarro–Frenk–White (NFW) profile (Navarro et al. 1996) with $r_s$ and $\rho_s$ as its scale radius and density, respectively. The boundary conditions are $M_\chi = 0$ at $r = 0$, $M_\chi = M_{200}$ and $L_\chi = 0$ at $r = r_{200}$, where $M_{200}$ and $r_{200}$ are the virial halo mass and radius, respectively; they are are equivalent to $r_s$ and $\rho_s$ in specifying a halo for a given redshift $z$. We adopt the baryon mass profile $M_b(r) \approx 0.1(4\pi\rho_s r_s^3)(r/r_s)^{0.6}$, based on cosmological hydrodynamical simulations of protogalaxies at $z \sim 17$ (Wise et al. 2008); see Appendix A. As an approximation, we assume the baryon mass profile is static and it does not evolve with time. We recast the fluid equations with dimensionless variables and solve them numerically using the method as in Balberg et al. (2002), Pollack et al. (2015), and Essig et al. (2019). The fiducial quantities relevant for later discussions are $M_0 = 4\pi\rho_s r_s^3$, $t_0 = 1/\sqrt{4\pi G\rho_s}$, and $(\sigma/m)_0 = 1/(r_s\rho_s)$; hence $M_b(r) = 0.1M_0(r/r_s)^{0.6}$. We then map dimensionless outputs
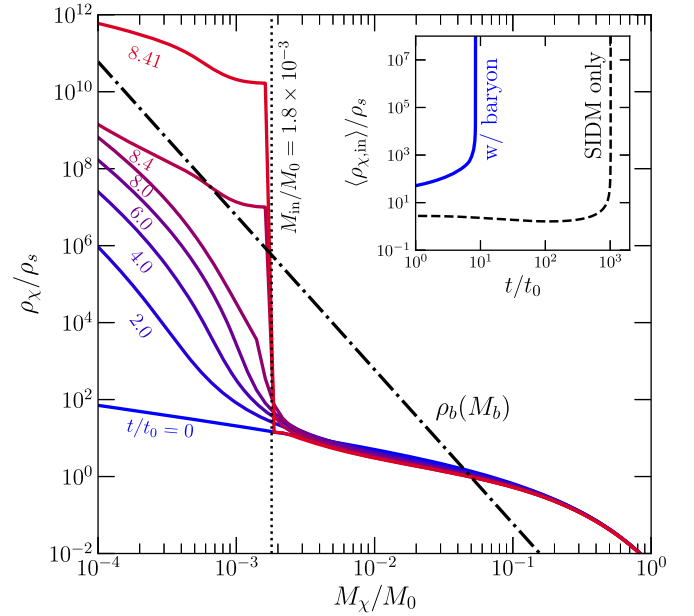


**Figure 1.** Gravothermal evolution of the dark matter density versus enclosed mass in the presence of the baryonic potential (solid), as well as the fixed baryon profile (dashed–dotted). Each dark matter profile is labeled with its corresponding evolution time, and the vertical dotted line indicates the mass of the central halo that would eventually collapse into a seed black hole. The insert panel illustrates the evolution of the averaged dark matter density of the central halo with (solid) and without (dashed) including the baryons.

from the simulations to physical ones assuming Planck cosmology, i.e., $h = 0.67$, $\Omega_m = 0.315$, and $\Omega_\Lambda = 0.685$ (Aghanim et al. 2020).

We further elaborate our assumptions made above. The initial halo is optically thin at its characteristic radius if $(\sigma/m)(r_s\rho_s) < 1$ (Pollack et al. 2015). Our numerical study takes $(\sigma/m)(r_s\rho_s) = 0.2$, and hence an NFW initial condition is well justified. As a concrete example, we take the simulated baryon profile from Wise et al. (2008), which is based on collisionless dark matter. In SIDM, the baryon profile could be diffuse because of halo core formation (Vogelsberger et al. 2014; Cruz et al. 2020). However, if baryon infall occurs early before a large core forms, the baryon distribution can be as compact as the one predicted in the collisionless limit (Robertson et al. 2018), or even more dense if SIDM collapse occurs (Sameie et al. 2021), albeit both simulations focus on systems at low redshifts.

Our approximation of a static baryon mass profile could be conservative in estimating the collapse time as the baryons would further contract when the collapse starts; see Sameie et al. (2021). We have also used a Hernquist profile (Hernquist 1990) to model the baryon distribution and obtained similar results if the baryons dominate the central potential as the simulated galaxies in Wise et al. (2008). Given these considerations, our model assumptions are justified. Nevertheless, it would be of interest to simulate high-$z$ protogalaxies in SIDM and test our assumptions in a cosmological environment.

## 3. Roles of Baryons

Figure 1 shows the gravothermal evolution of the dark matter density versus enclosed mass (solid) in the presence of the baryons (dashed–dotted), where we fix $(\sigma/m)(r_s\rho_s) = 0.2$. The insert panel illustrates the average inner density versus evolution time with (solid) and without (dashed) including the baryon mass. The average inner density $\langle\rho_{\chi,in}\rangle$ is calculated within the central region where the enclosed mass equals to that

of the seed black hole, as we will explain later. With the baryons, the halo does not form a large density core and it quickly evolves into the collapse phase (Sameie et al. 2018; Yang & Yu 2021). Its density keeps increasing and eventually becomes superexponential in the end. The collapse timescale is $t_c = 8.41 t_0$, a factor of $\sim 100$ shorter than the one predicted in the SIDM-only case with the same interaction strength. We also performed simulations with a Hernquist baryon profile and found a similar reduction factor in $t_c$ if the baryon distribution is as compact as that in Wise et al. (2008).

We also see that as the central density increases for $t \gtrsim 8.4 t_0$, the enclosed mass for a central region remains almost a constant $M_{\rm in} \approx 1.8 \times 10^{-3} M_0$. This is the region where the halo is in the short-mean-free-path regime. A similar phenomenon also occurs without including the baryons (Balberg et al. 2002). For the SIDM-only case we consider, the corresponding $M_{\rm in}/M_0$ value is $4.2 \times 10^{-2}$, which is larger than the one with the baryons. As the halo evolves further, the density continues increasing and the central halo ($Kn \lesssim 1$) would eventually collapse into a singular state, a seed black hole. We assume the seed mass $M_{\rm seed} = M_{\rm in}$, suggested by numerical studies of collapsed massive stars (Saijo et al. 2002).

## 4. Seeding Supermassive Black Holes

To explain the origin of high-$z$ SMBHs, the initial halo must be sufficiently heavy *and* collapse fast enough. We first check the scaling relations $M_{\rm in} \propto M_0 \propto M_{200}$ and $t_c \propto r_s^{-1} \rho_s^{-3/2} \propto M_{200}^{-1/3} c_{200}^{-7/2} (1+z)^{-7/2}$ (Essig et al. 2019), where $c_{200} = r_{200}/r_s$ is the halo concentration. Apparently, $t_c$ is very sensitive to $c_{200}$. There is a tight correlation between $c_{200}$ and $M_{200}$ for halos at $z \lesssim 5$, but the $c_{200}$ distribution at higher redshifts is less known. There is a trend that $c_{200}$ gradually becomes independent of $M_{200}$ and its median asymptote to $c_{200} \sim 3$ at $z \sim 5$–$10$ (Dutton & Macciò 2014; Zhao et al. 2009). We fix $c_{200} = 3$, and leave two parameters $M_{200}$ and $z$ to vary.

Figure 2 shows benchmarks (red) that could explain the origin of the SMBHs J1205−0000 with the Eddington ratio $f_{\rm Edd} = 0.16$ (upper panel; Onoue et al. 2019) and J1007+2115 with $f_{\rm Edd} = 1.06$ (lower panel; Yang et al. 2020b). The black curves indicate their Eddington accretion history reconstructed using Equation (1). For reference, the gray ones denote the accretion history of other high-$z$ SMBHs with $f_{\rm Edd} \sim 0.1$ (upper; Matsuoka et al. 2019; Onoue et al. 2019) and those $f_{\rm Edd} \sim 1$ (lower; Mortlock et al. 2011; Wu et al. 2015; Bañados et al. 2018; Wang et al. 2018; Yang et al. 2020b). We have checked that all of them (gray) could also be explained within our scenario. The direct collapse of pristine gas could provide massive enough seeds (magenta) for the SMBHs with $f_{\rm Edd} \sim 1$, but not those with $f_{\rm Edd} \sim 0.1$ (Onoue et al. 2019).

As the redshift of the initial halo increases, the favored halo mass becomes smaller, because the seed black hole has more time to grow. To explain the origin of the SMBHs with $f_{\rm Edd} \sim 1$, the mass is in a range of $M_{200} \sim 10^9$–$10^{11} M_\odot$ for $z \sim 11$–$9$. For those with $f_{\rm Edd} \sim 0.1$, $M_{200}$ needs to be relatively higher, $\sim 10^{11}$–$10^{12} M_\odot$, as their growth rate is much smaller and a heavier seed is required. We have checked that the overall trend holds for halos with $z \gtrsim 11$.

As an example, we take the case with $(M_{200}/M_\odot, z) = (6.8 \times 10^{11}, 8)$ that seeds J1205−0000, the most challenging SMBH, to demonstrate our derivation. For the halo, $\rho_s \approx 8.1 \times 10^7 M_\odot\,{\rm kpc}^{-3}$ and $r_s \approx 10\,{\rm kpc}$. Hence the fiducial parameters are $t_0 = 15\,{\rm Myr}$, $M_0 = 1.1 \times 10^{12} M_\odot$, and $(\sigma/m)_0 = 5.8\,{\rm cm}^2\,{\rm g}^{-1}$.
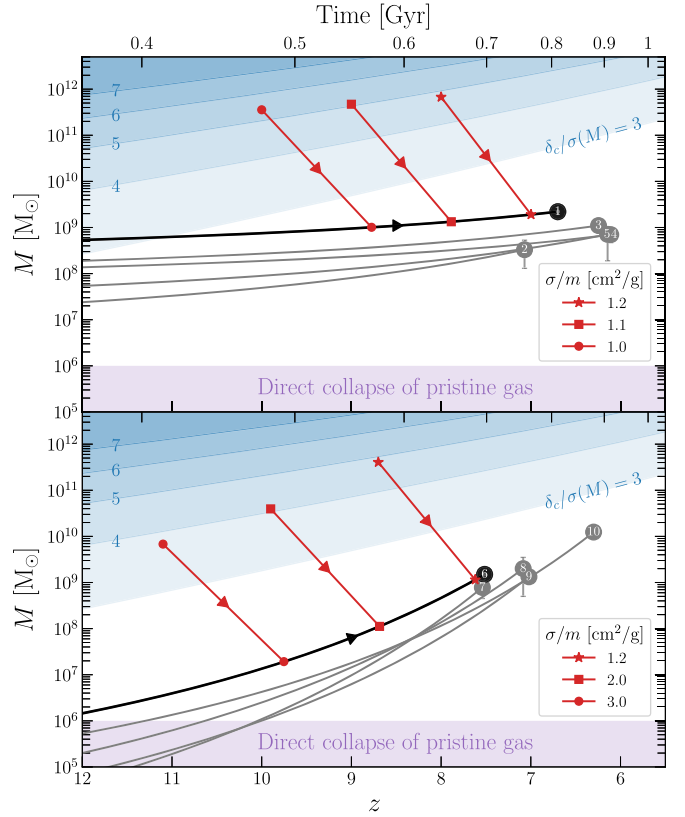


**Figure 2.** SIDM benchmarks (red) that could explain the origin of the SMBHs J1205−0000 (labeled as "1"; upper panel) and J1007+2115 ("6"; lower panel) with an observed Eddington growth rate of $f_{\rm Edd} = 0.16$ (Onoue et al. 2019) and 1.06 (Yang et al. 2020b), respectively. The black curves indicate their Eddington accretion history. For each red arrow, the markers on the higher- and lower-$z$ ends denote initial halo and seed masses, respectively, and the horizontal difference between the two ends indicates the timescale of gravothermal collapse. The blue shaded regions indicate the ratio of the critical density fluctuation to the halo mass variance. The magenta bands denote the mass range of the seed produced via the direct collapse of pristine gas. The gray curves are Eddington growth history of other high-$z$ SMBHs with $f_{\rm Edd} \sim 0.1$ (upper) and $\sim 1$ (lower).

The seed mass is $M_{\rm in} = 1.8 \times 10^{-3} M_0 \approx 1.9 \times 10^9 M_\odot$ and the collapse time $t_c = 8.4 t_0 \approx 124\,{\rm Myr}$, and the self-scattering cross section $\sigma/m \approx 1.2\,{\rm cm}^2\,{\rm g}^{-1}$. Since $z = 8$ is equivalent to $t = 642\,{\rm Myr}$ after the Big Bang, the seed forms at $766\,{\rm Myr}$ ($z = 7$). For an SIDM-only halo with the same parameters, we find $t_c \approx 10^3 t_0 \approx 15\,{\rm Gyr}$, too long to form a seed.

To speed up the collapse process in the absence of the baryonic influence, one would need to take much larger $\sigma/m$ and $c_{200}$ (Pollack et al. 2015), or consider dissipative self-interactions (Choquette et al. 2019; Essig et al. 2019; Huo et al. 2020). For comparison, our scenario predicts $\sigma/m \sim 1\,{\rm cm}^2\,{\rm g}^{-1}$ within a minimal elastic SIDM model that has been shown to explain dark matter distributions in the spirals (Ren et al. 2019), Milky Way satellites (Sameie et al. 2020), and dark-matter-deficient galaxies (Yang et al. 2020a). It is important to note dwarf galaxies at present that favor a large density core are those with diffuse baryon distributions (Kaplinghat et al. 2020). Thus their host SIDM halos would still be in the core-expansion phase and a shallow density profile is expected. In addition, in many well-motivated particle physics realizations of SIDM (see Tulin & Yu 2018), the cross section diminishes toward cluster scales. Thus, the stringent bounds on $\sigma/m$ from

galaxy clusters (Kaplinghat et al. 2016; Andrade et al. 2020) can be avoided.

## 5. Density Fluctuations

For the benchmark cases, the halo mass is in the range of $10^9–10^{12} M_\odot$ for $z \sim 11–8$. We use the standard Press–Schechter formalism (Press & Schechter 1974) to examine conditions for realizing those halos in the early universe. The halo mass function scales as $dn(M, z)/dM \propto \exp[-\delta_c^2(z)/2\sigma^2(M)]$ (Mo et al. 2010), where $\delta_c(z)$ is the critical density fluctuation at $z$ and $\sigma(M)$ the mass variance. We shaded the regions with various values of $\delta_c(z)/\sigma(M)$ in Figure 2 (blue). As expected, the halo mass increases as the density fluctuation increases and more massive halos form at later times.

The halos for seeding the SMBHs with a sub-Eddington (Eddington) accretion rate correspond to $\delta_c(z)/\sigma(M) \sim 4–6$ (3–5). In addition, the baryon concentration of host galaxies needs to be high as well such that the gravothermal collapse could occur fast enough. Thus our scenario predicts that high-$z$ SMBHs should be rare. Indeed, observations show they are extremely rare in the universe. Quasar surveys indicate that the number density of luminous ($L_{\rm AGN} \gtrsim 10^{46} \, {\rm erg \, s^{-1}}$) high-$z$ SMBHs with $M_{\rm BH} \sim 10^9 M_\odot$ is $\lesssim 10^{-7} \, {\rm Mpc^{-3}}$ (Kulkarni et al. 2019; Inayoshi et al. 2020; Trakhtenbrot 2020). The ratio of their mass to the dynamical (gas+stars) mass is $M_{\rm BH}/M_b \sim 1/100–1/30$ (Trakhtenbrot 2020). Taking $M_b/M_{200} \sim 0.2$, we find $M_{\rm BH}/M_{200} \sim (2–7) \times 10^{-3}$, broadly consistent with our prediction. We also note that baryon infall can occur for a halo heavier than $5 \times 10^3[(1 + z)/10]^{1.5} M_\odot$ (Mo et al. 2010), and all of the benchmarks satisfy this condition easily.

## 6. Angular Momentum

The angular momentum remnant of the inner halo could counter gravity and even slow down the gravothermal collapse. Besides, there is an upper limit on the specific angular momentum of a black hole, $J_{\rm BH}/M_{\rm BH} \leqslant (G/c)M_{\rm BH} \approx 1.4 \times 10^{-4}(M_{\rm BH}/10^7 M_\odot) \, {\rm kpc \, km \, s^{-1}}$ (Kerr 1963). Consider the benchmark with $(M_{200}/M_\odot, z) = (6.8 \times 10^{11}, 8)$ again, dark matter particles within the radius $r_{\rm in} = 0.063 r_s \approx 0.63$ kpc of the initial NFW halo would collapse to a seed, where the total enclosed mass is $M_{\rm in}$. We find $J_\chi/M_{\rm in} \approx 8 \, {\rm kpc \cdot km \, s^{-1}}$ for the halo within $r_{\rm in}$, based on a universal fitting formula (Liao et al. 2017). This is a factor of 100 larger than the allowed value for a $10^9 M_\odot$ seed.

Fortunately, dark matter self-interactions that lead to heat conductivity also induce viscosity, which dissipates the angular momentum remnant. In the long-mean-free-path regime, we find decays as

$$J_\chi^f \approx J_\chi^i \exp\left[-\frac{8}{\sqrt{27\pi}} \int dt \, \frac{\rho_\chi(\sigma/m)\nu_\chi^3 r_{\rm in}}{kGM_\chi}\right], \quad (3)$$

where $J_\chi^i$ and $J_\chi^f$ are the initial and final angular momenta of the central halo within $r_{\rm in}$, respectively, and $k = 2(\beta + 3)/3(\beta + 5)$ for a power law of $\rho_\chi \propto r^\beta$; see Appendix C. For an NFW (cored) profile, $\beta = -1$ (0) and hence $k = 1/3$ (2/5). Consider the benchmark, we have $r_{\rm in} = 0.063 r_s$, $M_\chi = M_{\rm in} = 1.8 \times 10^{-3} M_0$, $\rho_\chi(r_{\rm in}) = 14\rho_s$, $\sigma/m = 0.2/(r_s\rho_s)$, and $\nu_\chi(r_{\rm in}) \approx 0.48\sqrt{4\pi G\rho_s} r_s$. Taking $k = 1/3$, we find the timescale for achieving $J_\chi^f \sim 10^{-2} J_\chi^i$ is $\Delta t \approx 0.17 t_0$, much shorter than that
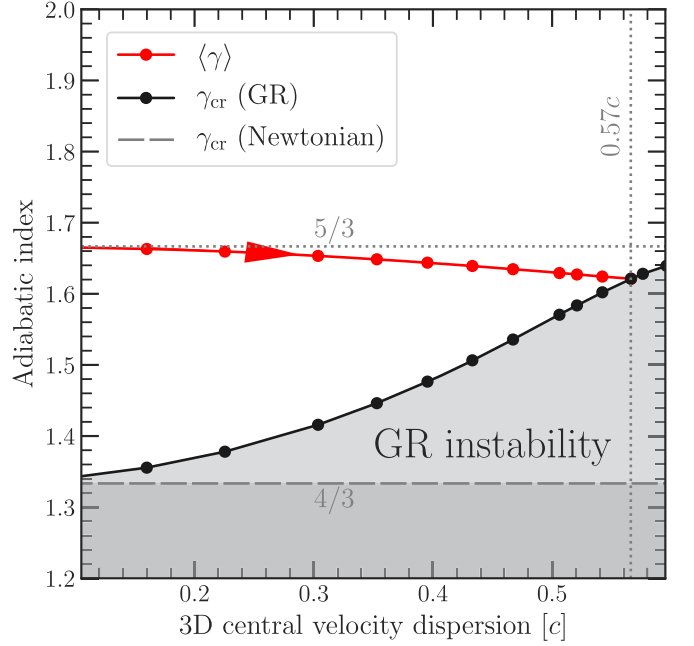


**Figure 3.** The pressure-averaged adiabatic index $\langle\gamma\rangle$ (red) and the critical index $\gamma_{\rm cr}$ (black) versus the central 3D velocity dispersion for each GR configuration (dot). When $\langle\gamma\rangle < \gamma_{\rm cr}$, the system triggers the GR instability. In the Newtonian limit, $\langle\gamma\rangle = 5/3$ for a monatomic ideal gas, and the instability condition is $\langle\gamma\rangle < 4/3$.

of gravothermal collapse $t_c = 8.4 t_0$. We have checked that the other five benchmarks in Figure 2 satisfy the dissipation condition. In SIDM, viscosity and conductivity share the same microscopic nature, and both effects are critical for seeding the SMBHs in our scenario.

## 7. Relativistic Instability

As the central density increases, the velocity dispersion of the collapsed central region increases as well (Balberg et al. 2002), and it would eventually approach the relativistic limit. To see the fate of the central halo where $Kn \lesssim 1$, we examine conditions for reaching GR instability. Motivated by early studies on globular cluster systems (King 1966; Merafina & Ruffini 1989), we assume that the number density of SIDM particles in the central halo at late stages follow a truncated Maxwell–Boltzmann distribution

$$dn(r) \propto \begin{cases} (e^{-\epsilon/k_B T} - e^{-\epsilon_c/k_B T})d^3p(\epsilon) & (\epsilon \leqslant \epsilon_c) \\ 0 & (\epsilon > \epsilon_c), \end{cases} \quad (4)$$

where $T$, $\epsilon$, and $p$ are temperature, energy, and momentum, respectively, and $\epsilon_c$ is the cutoff energy, above which the particle escapes to the boundary. Given the distribution in Equation (4), we use the method in Merafina & Ruffini (1989) and solve the Tolman–Oppenheimer–Volkov equation to find density and pressure profiles for the collapsed central region, where we impose the boundary condition $k_B T = 0.1 \, mc^2$. For each configuration, we follow Chandrasekhar's criterion (Chandrasekhar 1964), and calculate the critical adiabatic index $\gamma_{\rm cr}$ and the pressure-averaged adiabatic index $\langle\gamma\rangle$. The sufficient condition for the system to collapse into a black hole is $\langle\gamma\rangle < \gamma_{\rm cr}$. We will discuss technical details in a companion paper (W.-X. Feng et al. 2021, in preparation).

Figure 3 shows the averaged adiabatic index $\langle\gamma\rangle$ (red) and the critical index $\gamma_{\rm cr}$ (black) versus 3D velocity dispersion at

the center for each configuration denoted as a dot. As the velocity dispersion increases, its averaged index $\langle\gamma\rangle$ gradually decreases from its nonrelativistic limit for monatomic ideal gas 5/3 toward the ultrarelativistic limit 4/3. In contrast, the critical index $\gamma_{cr}$ increases from the Newtonian limit 4/3 (Shapiro & Teukolsky 1983). This is because as the pressure starts to dominate the energy density toward the GR limit, it destabilizes the system instead. The relativistic instability occurs when the 3D central velocity dispersion approaches $0.57c$ and $\langle\gamma\rangle = \gamma_{cr} \approx 1.62$, at which the corresponding fractional binding energy is 0.033 (W.-X. Feng et al. 2021, in preparation).

## 8. Conclusions

We have presented a scenario that could explain the origin of high-$z$ SMBHs with Eddington *and* sub-Eddington accretion rates. The presence of baryons in protogalaxies could deepen the gravitational potential and expedite the gravothermal collapse of an SIDM halo. The favored self-scattering cross section is broadly consistent with the one used to explain diverse dark matter distributions of galaxies. In this scenario, dark matter self-interactions induce viscosity that dissipates the angular momentum remnant of the central halo. The initial halo must be on high tails of density fluctuations, which may explain why high-$z$ SMBHs are extremely rare in observations. We also checked that the GR instability condition can be satisfied. The upcoming and future facilities are expected to search for quasars with a wide range of luminosities (Trakhtenbrot 2020). The observations would provide a more complete picture of populations of high-$z$ SMBHs and further test our scenario.

## Appendix A
## The Gas Density Profile

To model the gas distribution of protogalaxies, we adopt simulation results in Wise et al. (2008) (simulation B). Their simulated gas and dark matter distributions are fitted with a single power law of $\rho_b \sim r^{-2.4}$ and an NFW profile, respectively. We find the following ansatz works well for the gas:

$$\rho_b(r) = \rho_{b,s}\left(\frac{r}{r_s}\right)^{-2.4}, \qquad (A1)$$

where $\rho_{b,s}$ is the scale density of the gas and $r_s$ is the scale radius of the simulated halo. The corresponding mass profile is

$$M_b(r) = 1.67 \times \frac{\rho_{b,s}}{\rho_s}(4\pi\rho_s r_s^3)\left(\frac{r}{r_s}\right)^{0.6}. \qquad (A2)$$

We use simulation data shown in Figure 4 (right, panel b) of Wise et al. (2008) to fix the model parameters, $r_s = 73$ pc, $\rho_s = 2.6\,M_\odot\,\mathrm{pc}^{-3}$, and $\rho_{b,s} = 0.19\,M_\odot\,\mathrm{pc}^{-3}$; see Figure 4 for comparison. Since $1.67 \times \rho_{b,s}/\rho_s \approx 0.1$, we take $M_b(r) = 0.1M_0(r/r_s)^{0.6}$ for the static baryon distribution in our semianalytical simulations, shown as the dashed–dotted line in the left panel of Figure 5. Note
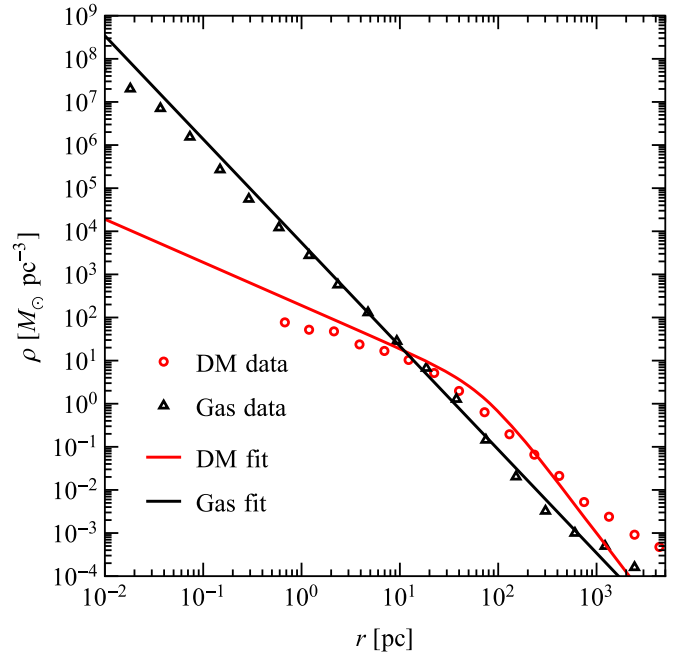


**Figure 4.** Dark matter (red) and gas (black) density profiles after fitting to the simulated ones in Wise et al. (2008); see their Figure 4 (right, panel b).
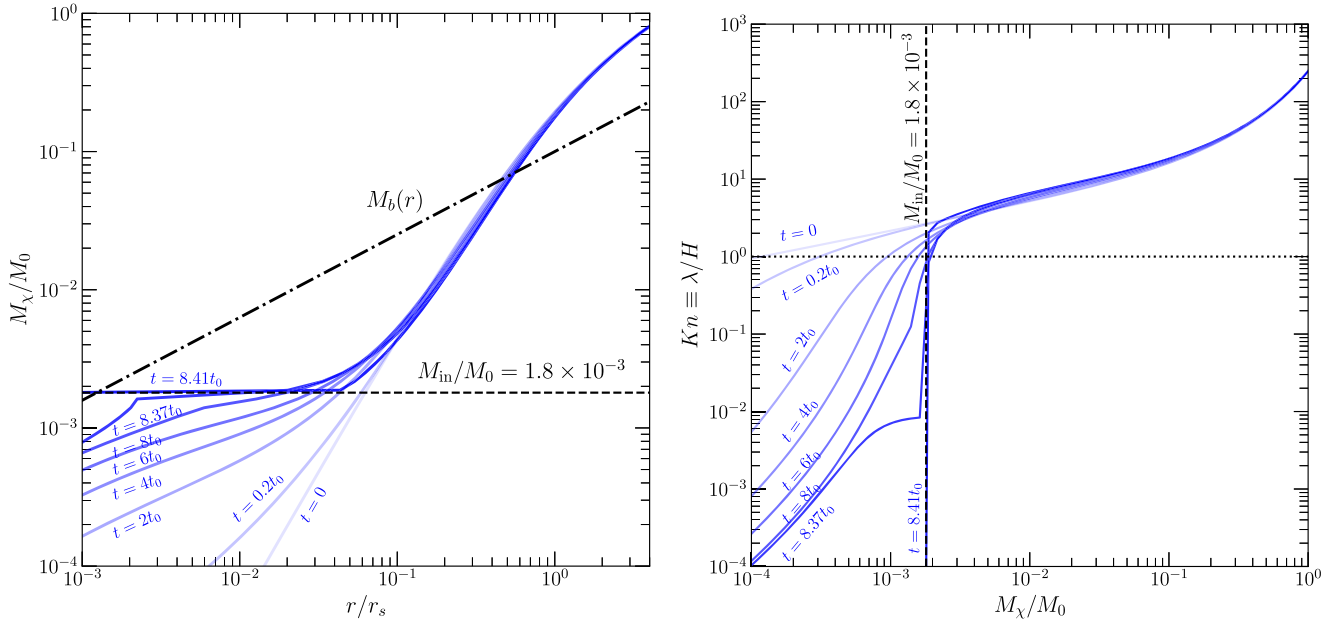
**Figure 5.** Left: evolution of dark matter mass profiles (solid) with $(\sigma/m)r_s\rho_s = 0.2$, together with the fixed baryon mass profile (dashed–dotted). Each dark matter profile is labeled with its corresponding evolution time. The dashed line indicates the mass of the central halo with $Kn < 1$. Right: corresponding $Kn$ value versus enclosed mass. The dotted horizontal line indicates $Kn = 1$, the boundary between short- and long-mean-free-path regimes, where $Kn < 1$ and $> 1$, respectively.

that the results from Wise et al. (2008) have high enough resolutions for setting initial conditions in our simulations, where we trace the collapse process with the conducting fluid model.

## Appendix B
## The Numerical Procedure

The procedure of our semianalytical simulations is largely based on the treatment given in Balberg et al. (2002), Pollack et al. (2015), and Essig et al. (2019). We first translate a relevant physical quantity $x$ to a dimensionless one $\hat{x}$ as $\hat{x} = x/x_0$, where $x_0$ is its corresponding fiducial value built from the halo parameters $\rho_s$ and $r_s$, as shown in Table 1.

The self-gravitating halo is segmented to $N = 182$ evenly log-spaced concentric shells in radius $\{\hat{r}_1, \hat{r}_2, \cdots, \hat{r}_N\}$ with $\hat{r}_1 = 10^{-4}$ and $\hat{r}_N = 100$. The halo is assumed to be in a quasi-hydrostatic equilibrium, and each shell is assumed to be in its local thermal equilibrium. The values of extensive quantities $(\hat{M}_i, \hat{L}_i)$ and intensive quantities $(\hat{\rho}_i, \hat{\nu}_i)$ are taken as the value at $\hat{r}_i$ and the average between values at $\hat{r}_i$ and $\hat{r}_{i-1}$, respectively. We fix the baryon mass profile $\hat{M}_{b,i}$ as

$$\hat{M}_{b,i} = \hat{M}_b(\hat{r}_i) = 0.1 \times \hat{r}_i^{0.6}. \tag{B1}$$

Consequently, we only use *one* set of Lagrangian zone radius for the halo through the simulations and dynamically update the enclosed baryon mass according to Equation (B1). The workflow is as follows:

1. Compute the initial 1D velocity dispersion profile $\hat{\nu}_{\chi,i}$ based on the input $\hat{r}_i$, $\hat{\rho}_{\chi,i}$, and $\hat{\rho}_{b,i}$ under the hydrostatic equilibrium condition,

$$\frac{\partial(\hat{\rho}_\chi \hat{\nu}_\chi^2)}{\partial \hat{r}} = -\frac{(\hat{M}_\chi + \hat{M}_b)\hat{\rho}_\chi}{\hat{r}^2}. \tag{B2}$$

2. Compute the luminosity profile $\hat{L}_{\chi,i}$ based on $\hat{r}_i$, $\hat{\rho}_{\chi,i}$, $\hat{\nu}_{\chi,i}$, and $\hat{\sigma}$ according to Equation (2) of the main text.

**Table 1**
Fiducial Quantities Used in Our Numerical Simulations

| | |
|---|---|
| $M_0 = 4\pi\rho_s r_s^3$ | $(\sigma/m)_0 = (r_s\rho_s)^{-1}$ |
| $\nu_0 = (4\pi G\rho_s)^{1/2}r_s$ | $L_0 = (4\pi)^{5/2}G^{3/2}\rho_s^{5/2}r_s^5$ |
| $t_0 = (4\pi G\rho_s)^{-1/2}$ | |

3. Allow a small passage of time $\Delta\hat{t}$ and compute the specific energy change $\Delta\hat{u}_{\chi,i}$, $\hat{u}_{\chi,i} \equiv 3\hat{\nu}_{\chi,i}^2/2$, due to heat conduction,

$$\frac{\Delta\hat{u}_{\chi,i}}{\Delta\hat{t}} = -\left(\frac{\partial\hat{L}_\chi}{\partial\hat{M}_\chi}\right)_i, \tag{B3}$$

where the dark matter density is fixed. We then update $\hat{u}_{\chi,i}$ with $\hat{u}_{\chi,i} + \Delta\hat{u}_{\chi,i}$. The time step $\Delta\hat{t}$ is sufficiently small, i.e., $|\Delta\hat{u}_{\chi,i}/\hat{u}_{\chi,i}| < 10^{-4}$. such that the linear approximations used in step 4 below are valid.

4. Upon updating $\hat{u}_{\chi,i}$, the $i$th dark matter halo shell is no longer virialized. To return to hydrostatic equilibrium, we perturb $\hat{r}_i$, $\hat{\rho}_{\chi,i}$, and $\hat{\nu}_{\chi,i}$, while keeping the mass $\hat{M}_{\chi,i}$ and specific entropy $\hat{s}_{\chi,i} = \ln(\hat{\nu}_{\chi,i}^3/\hat{\rho}_{\chi,i})$ of the shell fixed. We treat mass conservation, specific entropy conservation, kinetic energy conservation, and hydrostatic equilibrium relations, shown in the main text, at the linear order and solve them for all shells simultaneously. For the hydrostatic equilibrium relation, we take the sum of $\hat{M}_{\chi,i}$ and $\hat{M}_{b,i} = \hat{M}_b(\hat{r}_i)$ to compute the gravitational potential. For numerical accuracy, we iteratively perform the perturbation 10 times until hydrostatic equilibrium is established everywhere.

5. Reestablishing hydrostatic equilibrium gives new values for $\hat{r}_i$, $\hat{\rho}_{\chi,i}$, and $\hat{\nu}_{\chi,i}$. We return to step 1 and update the luminosity $\hat{L}_i$.

6. Track the Knudsen number $Kn \equiv \lambda/H$ for the innermost shell. The evolution is terminated when $Kn$ drops below $10^{-4}$.

The above procedure is coded in C++ with the eigen 3.2 library for linear algebra (Guennebaud et al. 2010).

In Figure 5, we show evolution of dark matter mass profile (left panel) and the corresponding $Kn$ value versus enclosed mass (right panel). These results are complementary to those presented in Figure 1 of the main text.

## Appendix C
## Angular Momentum Dissipation

Dark matter self-interactions provide an important avenue to transport angular momentum. To estimate this effect, we keep track of the collapsing central halo in a Lagrangian zone manner, i.e., the number of particles in each mass sphere is conserved, while allowing its corresponding radius to change over the evolution. This is consistent with the method we use for solving the conduction fluid equations. We further assume the mass distribution is spherically symmetric, which is particularly motivated in SIDM (Dave et al. 2001; Peter et al. 2013), and write the moment of inertia as $I_\chi = kM_{\rm in}r_{\rm in}^2$, where $k = 2(\beta+3)/3(\beta+5)$ for a power law of $\rho_\chi \propto r^\beta$. For an NFW profile, $\beta = -1$ and $k = 1/3$. For a density core, we have $\beta = 0$ and $k = 2/5$. The angular momentum is given by

$$J_{\chi,{\rm in}} = I_\chi \omega = kM_{\rm in}r_{\rm in}^2\omega \simeq {\rm const.}, \qquad (C1)$$

where $\omega$ is the rotational frequency of the inner region and $r_{\rm in}$ is its boundary that changes with time. This leads to

$$\frac{d}{dt}(r_{\rm in}\omega) = \frac{d}{dt}\left(\frac{J_{\chi,{\rm in}}}{kM_{\rm in}r_{\rm in}}\right) \simeq -\frac{J_{\chi,{\rm in}}}{kM_{\rm in}r_{\rm in}^2}\left(\frac{dr_{\rm in}}{dt}\right). \qquad (C2)$$

The bulk velocity is $v_\phi = r_{\rm in}\omega\sin\theta$ along the $\phi$-direction of the rotational axis. $\theta$ is the polar angle. The bulk velocity increases (decreases) $dv_\phi/dt > 0 \, (<0)$ as the boundary of the inner region shrinks (expands) $dr_{\rm in}/dt < 0 \, (>0)$. An increase in $v_\phi$ will drag the ambient regions just outside the boundary and exert a shear pressure on the boundary bulk surface,

$$\frac{1}{A_{\rm in}}\frac{d}{dt}(N_{r_{\rm in}}mv_\phi)_\pm = \mp\eta_{r_{\rm in}}\frac{dv_\phi}{dr_{\rm in}}, \qquad (C3)$$

where $m$ is the dark matter particle mass, $A_{\rm in} = 4\pi r_{\rm in}^2$ is the surface area of the inner region, $\eta_{r_{\rm in}} \equiv \eta(r_{\rm in})$ is the viscosity of the SIDM fluid, and $N_{r_{\rm in}}$ is number of particles, on the bulk surface. The subscript $+/-$ indicates if the quantity increases/decreases. Given the Lagrangian zone setup, $N_{r_{\rm in}}$ is a constant through the evolution, and from Equation (C3) we can show

$$\left(\frac{dr_{\rm in}}{dt}\right)_\mp = \mp\frac{4\pi r_{\rm in}^2\eta_{r_{\rm in}}}{N_{r_{\rm in}}m}. \qquad (C4)$$

The bulk momentum can be transported out through the shear pressure due to viscosity. Combining Equations (C2) and (C4), we obtain the rate of momentum transport to the surroundings:

$$\frac{d}{dt}(r_{\rm in}\omega)_\pm = \pm\frac{4\pi\eta_{r_{\rm in}}J_{\chi,{\rm in}}}{kM_{\rm in}N_{r_{\rm in}}m}.$$

As the total angular momentum is conserved, the *loss* of the angular momentum of the inner region (shrinking case) is given by

$$\frac{dJ_{\chi,{\rm in}}}{dt} \simeq -N_{r_{\rm in}}m\int\frac{d\Omega}{4\pi}\left[r_{\rm in}\sin\theta \times \frac{d}{dt}(r_{\rm in}\omega\sin\theta)\right]$$

$$= -\int\frac{\sin^3\theta d\theta d\phi}{4\pi}r_{\rm in}\frac{d}{dt}(N_{r_{\rm in}}mr_{\rm in}\omega)_+$$

$$= -\frac{8\pi}{3}\frac{J_{\chi,{\rm in}}}{kM_{\rm in}}\eta_{r_{\rm in}}r_{\rm in}. \qquad (C5)$$

We have

$$J_{\chi,{\rm in}}(t; M_{\rm in}) = J_{\chi,{\rm in}}^i\exp\left(-\frac{8\pi}{3}\int_{t_i}^t\frac{\eta_{r_{\rm in}}r_{\rm in}(t')}{kM_{\rm in}}dt'\right), \qquad (C6)$$

where $J_{\chi,{\rm in}}^i$ is the initial angular momentum of the inner region. As for conductivity (Balberg et al. 2002), the viscosity for both long-mean-free-path and short-mean-free-path regimes can be combined into a single expression,

$$\eta = \frac{1}{3}mn\bar{v}\left(\frac{1}{\lambda} + \frac{\nu t_r}{H^2}\right)^{-1}$$

$$= \frac{1}{3}\alpha(\sigma/m)\bar{v}\left[\alpha(\sigma/m)^2 + \frac{4\pi G}{\rho\nu^2}\right]^{-1}, \qquad (C7)$$

where we have used the gravitational scale height $H = \sqrt{\nu^2/4\pi G\rho}$, the mean free path $\lambda = 1/n\sigma$, and the relaxation time $t_r = 1/(\alpha n\nu\sigma)$ with number density $n$, cross section $\sigma$, and $\alpha = (16/\pi)^{1/2} \approx 2.26$ for hard spheres.

We evaluate $\eta$ at the boundary $r_{\rm in}$ and take $\bar{v} \simeq \sqrt{3}\,\nu$, and obtain

$$J_{\chi,{\rm in}} = J_{\chi,{\rm in}}^i\exp\left[-\frac{8}{\sqrt{27\pi}}\int_{t_i}^t\frac{\rho_{r_{\rm in}}(t')(\sigma/m)\nu_{r_{\rm in}}^3(t')r_{\rm in}(t')}{kGM_{\rm in}}dt'\right] \qquad (C8)$$

in the long-mean-free-path limit, and

$$J_{\chi,{\rm in}} = J_{\chi,{\rm in}}^i\exp\left[-\frac{8\pi}{3\sqrt{3}}\int_{t_i}^t\frac{\nu_{r_{\rm in}}(t')r_{\rm in}(t')}{kM_{\rm in}(\sigma/m)}dt'\right] \qquad (C9)$$

in the short-mean-free-path limit, where we have used the density $\rho_{r_{\rm in}} = \rho(r_{\rm in}) = mn(r_{\rm in})$ and $\nu_{r_{\rm in}} = \nu(r_{\rm in})$ the 1D velocity dispersion at the boundary.

For the benchmark discussed in Section 6, we estimate the characteristic timescale to dissipate the angular momentum remnant $\Delta t \sim 0.2t_0$ with fixed $M_{\rm in} = 1.8 \times 10^{-3}M_0$ and its corresponding $r_{\rm in} = 0.063r_s$, i.e., the radius at which the enclosed mass of the initial NFW halo is $M_{\rm in}$. We do not take into account the change in the radius of the mass sphere and the velocity dispersion, as they are negligible for $\Delta t \sim 0.2t_0$; see the left panel of Figure 5. The estimation is based on Equation (C8), and this is well justified as the collapsed region is in the long-mean-free-path regime at $r \sim r_{\rm in}$ for $\Delta t \sim 0.2t_0$, as shown in the right panel of Figure 5. For a sphere with smaller $M_{\rm in}$ more toward the center, the timescale is even shorter, as we can see from the scaling relation $\Delta t \sim GM_\chi/(\rho_\chi\nu_\chi^3 r\sigma/m)$. For an NFW halo, we have $\rho_\chi \propto r^{-1}$, $M_\chi \propto r^2$, $\nu_\chi \propto r^{0.2}$, and hence $\Delta t \propto r^{1.4}$. For a cored halo, $\rho_\chi \propto r^0$, $M_\chi \propto r^3$, $\nu_\chi \propto r^0$, and $\Delta t \propto r^2$. For both cases, $\Delta t$ decreases as $r$ reduces. Thus it is reasonable to collectively treat particles in the mass sphere $M_{\rm in} = 1.8 \times 10^{-3}M_0$, which would collapse to a seed, and estimate the overall timescale for dissipating angular momentum.

**Table 2**
The Sample of High-$z$ SMBHs Shown in Figure 2 of the Main Text

| Label | Name | $M_{BH}$ ($10^9 M_\odot$) | $z$ | $f_{Edd}$ | Ref. |
|---|---|---|---|---|---|
| 1 | J1205−0000 | $2.2^{+0.2}_{-0.6}$ | $6.699^{+0.007}_{-0.001}$ | $0.16^{+0.04}_{-0.02}$ | Onoue et al. (2019) |
| 2 | J1243+0100 | $0.33^{+0.2}_{-0.2}$ | $7.07^{+0.01}_{-0.01}$ | $0.34^{+0.02}_{-0.02}$ | Matsuoka et al. (2019) |
| 3 | J2239+0207 | $1.1^{+0.3}_{-0.2}$ | $6.245^{+0.008}_{-0.007}$ | $0.17^{+0.04}_{-0.05}$ | Onoue et al. (2019) |
| 4 | J2216−0016 | $0.7^{+0.14}_{-0.23}$ | $6.109^{+0.007}_{-0.008}$ | $0.15^{+0.05}_{-0.03}$ | Onoue et al. (2019) |
| 5 | J1208−0200 | $0.71^{+0.24}_{-0.52}$ | $6.144^{+0.008}_{-0.010}$ | $0.24^{+0.18}_{-0.08}$ | Onoue et al. (2019) |
| 6 | J1007+2115 | $1.5^{+0.2}_{-0.2}$ | $7.5149^{+0.0004}_{-0.0004}$ | $1.06^{+0.2}_{-0.2}$ | Yang et al. (2020b) |
| 7 | J1342+0928 | $0.78^{+0.33}_{-0.19}$ | $7.5413^{+0.0007}_{-0.0007}$ | $1.5^{+0.5}_{-0.4}$ | Bañados et al. (2018) |
| 8 | J1120+0641 | $2.0^{+1.5}_{-0.7}$ | $7.085^{+0.003}_{-0.003}$ | $1.2^{+0.6}_{-0.5}$ | Mortlock et al. (2011) |
| 9 | J0038−1527 | $1.33^{+0.25}_{-0.25}$ | $7.021^{+0.005}_{-0.005}$ | $1.25^{+0.19}_{-0.19}$ | Wang et al. (2018) |
| 10 | J0100+2802 | $12.4^{+1.9}_{-1.9}$ | $6.30^{+0.01}_{-0.01}$ | $0.99^{+0.22}_{-0.22}$ | Wu et al. (2015) |

## Appendix D
## The Adiabatic Index

We consider a perfect fluid with energy density $\rho(r)c^2$ and pressure $p(r)$ in a Schwarzschild metric (Chandrasekhar 1964)

$$ds^2 = -e^{2\Phi(r)}c^2 dt^2 + e^{2\Lambda(r)}dr^2 + r^2(d\theta^2 + \sin^2\theta\, d\phi^2),$$

where $e^{2\Phi} = \exp[2\int_r^\infty (dp/dr')/(p+\rho c^2)dr']$ and $e^{2\Lambda} = [1 - 2GM(r)/rc^2]^{-1}$. The critical adiabatic index is

$$\gamma_{cr} \equiv \frac{4}{3} + \frac{\int e^{3\Phi+\Lambda}[16p + (e^{2\Lambda}-1)(\rho+p)](e^{2\Lambda}-1)r^2 dr}{36\int e^{3\Phi+\Lambda}pr^2 dr}$$
$$+ \frac{4\pi G \int e^{3(\Phi+\Lambda)}[8p + (e^{2\Lambda}+1)(\rho c^2+p)]pr^4 dr}{9c^4 \int e^{3\Phi+\Lambda}pr^2 dr}$$
$$+ \frac{16\pi^2 G^2 \int e^{3\Phi+5\Lambda}(\rho c^2+p)p^2 r^6 dr}{9c^8 \int e^{3\Phi+\Lambda}pr^2 dr},$$

$$\text{(D1)}$$

and the pressure-averaged adiabatic index is $\langle\gamma\rangle \equiv \int e^{3\Phi+\Lambda}\gamma(r)pr^2 dr/(\int e^{3\Phi+\Lambda}pr^2 dr)$. These expressions are fully relativistic, and we will provide their derivations in a companion paper (W.-X. Feng et al. 2021, in preparation).

## Appendix E
## The Sample of High-$z$ SMBHs

In Table 2, we list high-$z$ SMBHs shown in Figure 2 of the main text, in the order of their labeling number in the figure. The Eddington ratio is calculated as $f_{Edd} = L_{bol}/L_{Edd}$, where $L_{bol}$ is the observed bolometric luminosity and $L_{Edd} = 1.3 \times 10^{38}$ $(M_{BH}/M_\odot)$ erg s$^{-1}$ is the Eddington luminosity.

## ORCID iDs

Wei-Xiang Feng ⓘ https://orcid.org/0000-0002-9048-2992
Hai-Bo Yu ⓘ https://orcid.org/0000-0002-8421-8597
Yi-Ming Zhong ⓘ https://orcid.org/0000-0001-9922-6162

## References

Aghanim, N., Akrami, Y., Ashdown, M., et al. 2020, A&A, 641, A6
Ahn, K.-J., & Shapiro, P. R. 2005, MNRAS, 363, 1092
Alexander, T., & Natarajan, P. 2014, Sci, 345, 1330
Andrade, K. E., Fuson, J., Gad-Nasr, S., et al. 2020, arXiv:2012.06611
Balberg, S., & Shapiro, S. L. 2002, PhRvL, 88, 101301
Balberg, S., Shapiro, S. L., & Inagaki, S. 2002, ApJ, 568, 475
Bañados, E., Venemans, B. P., Mazzucchelli, C., et al. 2018, Natur, 553, 473
Begelman, M. C. 1979, MNRAS, 187, 237
Begelman, M. C., Volonteri, M., & Rees, M. J. 2006, MNRAS, 370, 289
Bromm, V., & Loeb, A. 2003, ApJ, 596, 34
Chandrasekhar, S. 1964, ApJ, 140, 417
Choquette, J., Cline, J. M., & Cornell, J. M. 2019, JCAP, 2019, 036
Cruz, A., Pontzen, A., Volonteri, M., et al. 2020, MNRAS, 500, 2177
Dave, R., Spergel, D. N., Steinhardt, P. J., & Wandelt, B. D. 2001, ApJ, 547, 574
Dutton, A. A., & Macciò, A. V. 2014, MNRAS, 441, 3359
Essig, R., Mcdermott, S. D., Yu, H.-B., & Zhong, Y.-M. 2019, PhRvL, 123, 121102
Freese, K., Ilie, C., Spolyar, D., Valluri, M., & Bodenheimer, P. 2010, ApJ, 716, 1397
Guennebaud, G., Jacob, B., et al. 2010, Eigen v3, Zenodo, http://eigen.tuxfamily.org
Hernquist, L. 1990, ApJ, 356, 359
Huo, R., Yu, H.-B., & Zhong, Y.-M. 2020, JCAP, 2020, 051
Inayoshi, K., Visbal, E., & Haiman, Z. 2020, ARA&A, 58, 27
Kaplinghat, M., Ren, T., & Yu, H.-B. 2020, JCAP, 2020, 027
Kaplinghat, M., Tulin, S., & Yu, H.-B. 2016, PhRvL, 116, 041302
Kerr, R. P. 1963, PhRvL, 11, 237
King, I. R. 1966, AJ, 71, 64
Koda, J., & Shapiro, P. R. 2011, MNRAS, 415, 1125
Kulkarni, G., Worseck, G., & Hennawi, J. F. 2019, MNRAS, 488, 1035
Liao, S., Chen, J., & Chu, M.-C. 2017, ApJ, 844, 86
Lynden-Bell, D., & Wood, R. 1968, MNRAS, 138, 495
Matsuoka, Y., Onoue, M., Kashikawa, N., et al. 2019, ApJL, 872, L2
McKinney, J. C., Tchekhovskoy, A., Sadowski, A., & Narayan, R. 2014, MNRAS, 441, 3177
Merafina, M., & Ruffini, R. 1989, A&A, 221, 4
Mo, H., van den Bosch, F., & White, S. 2010, Galaxy Formation and Evolution (Cambridge: Cambridge Univ. Press)
Mortlock, D. J., Warren, S. J., Venemans, B. P., et al. 2011, Natur, 474, 616
Natarajan, P. 2011, BASI, 39, 145
Navarro, J. F., Frenk, C. S., & White, S. D. 1996, ApJ, 462, 563
Onoue, M., Kashikawa, N., Matsuoka, Y., et al. 2019, ApJ, 880, 77
Peter, A. H. G., Rocha, M., Bullock, J. S., & Kaplinghat, M. 2013, MNRAS, 430, 105
Pollack, J., Spergel, D. N., & Steinhardt, P. J. 2015, ApJ, 804, 131
Press, W. H., & Schechter, P. 1974, ApJ, 187, 425
Ren, T., Kwa, A., Kaplinghat, M., & Yu, H.-B. 2019, PhRvX, 9, 031020
Robertson, A., Massey, R., Eke, V., et al. 2018, MNRAS, 476, L20
Rocha, M., Peter, A. H., Bullock, J. S., et al. 2013, MNRAS, 430, 81
Sadowski, A., Narayan, R., Tchekhovskoy, A., et al. 2015, MNRAS, 447, 49
Saijo, M., Baumgarte, T. W., Shapiro, S. L., & Shibata, M. 2002, ApJ, 569, 349
Salpeter, E. 1964, ApJ, 140, 796
Sameie, O., Boylan-Kolchin, M., Sanderson, R., et al. 2021, arXiv:2102.12480
Sameie, O., Creasey, P., Yu, H.-B., et al. 2018, MNRAS, 479, 359

Sameie, O., Yu, H.-B., Sales, L. V., Vogelsberger, M., & Zavala, J. 2020, PhRvL, 124, 141102

Shakura, N. I., & Sunyaev, R. 1976, MNRAS, 175, 613

Shapiro, S., & Teukolsky, S. 1983, Black holes, White Dwarfs, and Neutron Stars: The Physics of Compact Objects (New York: Wiley)

Shapiro, S. L. 2005, ApJ, 620, 59

Spergel, D. N., & Steinhardt, P. J. 2000, PhRvL, 84, 3760

Trakhtenbrot, B. 2020, in IAU Symp. 356, Nuclear Activity in Galaxies Across Cosmic Time, ed. M. Pović et al. (Cambridge: Cambridge Univ. Press), 261

Tulin, S., & Yu, H.-B. 2018, PhR, 730, 1

Vogelsberger, M., Zavala, J., & Loeb, A. 2012, MNRAS, 423, 3740

Vogelsberger, M., Zavala, J., Simpson, C., & Jenkins, A. 2014, MNRAS, 444, 3684

Volonteri, M. 2010, A&ARv, 18, 279

Volonteri, M., & Rees, M. J. 2005, ApJ, 633, 624

Wang, F., Yang, J., Fan, X., et al. 2018, ApJL, 869, L9

Wise, J. H., Turk, M. J., & Abel, T. 2008, ApJ, 682, 745

Wu, X.-B., Wang, F., Fan, X., et al. 2015, Natur, 518, 512

Yang, D., & Yu, H.-B. 2021, arXiv:2102.02375

Yang, D., Yu, H.-B., & An, H. 2020a, PhRvL, 125, 111105

Yang, J., Wang, F., Fan, X., et al. 2020b, ApJL, 897, L14

Zhao, D., Jing, Y., Mo, H., & Boerner, G. 2009, ApJ, 707, 354